



A quantum dot in germanium proximitized by a superconductor

Received: 2 June 2024

Accepted: 2 December 2024

Published online: 10 February 2025

Check for updates

Lazar Lakic ^{1,4}, William I. L. Lawrie ^{1,4}, David van Driel², Lucas E. A. Stehouwer², Yao Su¹, Menno Veldhorst ², Giordano Scappucci ², Ferdinand Kuemmeth ^{1,3} & Anasua Chatterjee ^{1,2}

As one of the few group IV materials with the potential to host superconductor–semiconductor hybrid devices, planar germanium hosting proximitized quantum dots is a compelling platform to achieve and combine topological superconductivity with existing and new qubit modalities. We demonstrate a quantum dot in a Ge/SiGe heterostructure proximitized by a platinum germanosilicide (PtSiGe) superconducting lead, forming a superconducting lead–quantum dot–superconducting lead junction. We show tunability of the coupling strength between the quantum dot and the superconducting lead, and gate control of the ratio of charging energy and the induced gap, and we tune the ground state of the system between even and odd parity. Furthermore, we characterize critical magnetic field strengths, finding a critical out-of-plane field of 0.90 ± 0.04 T. Finally, we explore sub-gap spin splitting, observing rich physics in the resulting spectra, that we model using a zero-bandwidth model in the Yu–Shiba–Rusinov limit. Our findings open up the physics of alternative spin and superconducting qubits, and the physics of Josephson junction arrays, in germanium.

New and unexpected physical phenomena can emerge in superconducting–semiconducting hybrids, enabling engineered quantum materials¹, circuit quantum electrodynamics with promising superconducting qubit modalities^{2,3} and topologically protected phases^{4–6}. In particular, proximitized quantum dots (QDs) constitute key building blocks for devices such as Cooper pair splitters⁷, Kitaev chains^{5,6} and protected qubits^{8,9}. However, to date the majority of these experiments have been performed in group III–V materials, where nuclear spins are unavoidable, critically hampering spin coherence, and where two-dimensional (2D) heterostructures exhibit piezoelectricity, deleterious for circuit quantum electrodynamics circuits¹⁰. Conversely, silicon and germanium are established group IV material platforms that can integrate spin qubits hosted in gate defined QDs^{11,12}, with isotopic purification having proved crucial for ultra-long spin qubit coherence¹³. Contrary to silicon¹⁴, germanium forms low resistance ohmic contacts due to

intrinsic Fermi level pinning close to the valence band^{15,16}. This has motivated a strong effort to induce superconductivity^{17–22}, and very recently, signs of hard-gap superconductivity have been observed in mesoscopic devices implemented in a Ge/SiGe heterostructure^{21,22}, in Ge/Si core/shell nanowires^{23–25} and in a circuit quantum electrodynamics circuit²⁶.

Here we present a superconducting–semiconducting hybrid QD, which is hosted in Ge, a group IV material uniquely allowing for both isotopic purification²⁷ and a superconducting hard gap^{21,22}. Our demonstration in a 2D heterostructure establishes a promising platform that exhibits enhanced scalability compared to nanowires, is compatible with radiofrequency reflectometry readout²⁸ and is a highly successful spin qubit platform^{29,30}. It may therefore be useful for extending the range of qubit interactions by using crossed Andreev reflection^{31,32} as well as heterogeneous quantum processors^{8,33} incorporating spin^{11,12}.

¹Center for Quantum Devices, Niels Bohr Institute, University of Copenhagen, Copenhagen, Denmark. ²QuTech and Kavli Institute of Nanoscience, Delft University of Technology, Delft, The Netherlands. ³Institute of Experimental and Applied Physics, University of Regensburg, Regensburg, Germany.

⁴These authors contributed equally: Lazar Lakic, William I. L. Lawrie. e-mail: anasua.chatterjee@tudelft.nl

and superconducting circuits³⁴. Isotopically purified, proximitized germanium may enable coherent Andreev spin qubits, protected superconducting qubits and QD-based Kitaev chains, and our demonstration of a QD with gate-tunable proximitization in a group IV heterostructure is a key ingredient.

In this work, superconducting polycrystalline platinum–germanium–silicide (PtSiGe) leads are formed by a controlled thermally activated solid phase reaction between deposited platinum (Pt) and the heterostructure (Ge/SiGe)²¹. Importantly, the PtSiGe leads alleviate the need to etch into the heterostructure to deposit or pattern the superconductor, a potential source of damage exposing the quantum well and interface to oxygen and processing. This method of achieving a transparent interface to a superconductor, via a reaction with a deposited noble metal, constitutes a general technique that has been exploited in other materials^{35–37}. The leads act as charge reservoirs and as a source of proximitization for the QD. We first demonstrate Coulomb blockade physics of a QD coupled to two superconducting leads (SCs) forming a SC–QD–SC junction. We identify a superconducting gap energy window of $4\Delta_0 = 284$ μeV, where Δ_0 is the superconducting pairing amplitude, inside of which transport is suppressed, and outside of which standard Coulomb diamonds are recovered. The charging energy of the system is typically larger than 1 meV, making it the dominating energy scale. Consequentially, Yu–Shiba–Rusinov (YSR) physics is expected to describe the observed phenomena. We observe sub-gap states in transport upon increasing the QD–SC coupling Γ_s , which is consistent with the formation of YSR states in the system^{38,39}. We demonstrate gate control of Γ_s by tuning the ground state at half-filling from a singlet state to a doublet state⁴⁰. We then study the critical magnetic field of the hybrid device, finding an out-of-plane critical magnetic field $B_{c,\perp} = 0.90 \pm 0.04$ T. Finally, we investigate spin splitting in the SC–QD–SC system, finding a *g*-factor of 1.5 ± 0.2 for an out-of-plane magnetic field, and also characterize the *g*-tensor anisotropy. To explain the energy splitting observed in the SC–QD–SC system, we use a zero-bandwidth (ZBW) Anderson impurity model^{41,42} with the possibility of Zeeman splitting on the SC. Our observation of controllable sub-gap states and sub-gap spin splitting, magnetic field resilience and the high tunability of the QD–SC coupling establishes Ge/SiGe and PtSiGe as an attractive platform for hybrid quantum information processing.

We use established fabrication protocols for QD fabrication⁴³ and the superconducting contacts²¹ in Ge/SiGe quantum wells⁴⁴, to create a QD coupled to two SCs formed by rapid thermal annealing of Pt at 400 °C in an Ar atmosphere for 15 min. Figure 1a shows a false-coloured scanning electron micrograph of the device, consisting of one lithographically defined layer for the SCs (cyan) and two layers of electrostatic gates (yellow and orange; Methods and section I for further details). Figure 1b shows a schematic of the cross-section of the device heterostructure and gate stack. Layers are electrically isolated from one another by 7 nm of Al₂O₃ deposited by atomic layer deposition at 150 °C. Barrier gates (left, LB and right, RB) control Γ_s , while the plunger gate (PG) controls the relative electrochemical potential of the QD levels with respect to the SCs (ϵ_0) as seen in Fig. 1c. Two gates (helper gate, HG and cut-off gate, CO) are also used to confine (HG) the QD and prevent unwanted accumulation (CO). We use standard d.c. transport and low-frequency lock-in techniques to measure source–drain current I_{SD} and differential conductance G in units of conductance quanta ($2e^2/h$), where e is the elementary charge and h is Planck's constant, across the QD. Notably, our device is also connected to a radiofrequency reflectometry circuit via the source SC; both techniques are described in Supplementary Section I. Additional datasets in the low-coupling regime measured using this radiofrequency probe are presented in Supplementary Section II.

All data are taken at a lock-in frequency of 119 Hz and amplitude of 2.5 μV. Figure 1d shows I_{SD} as a function of the tunnel barriers V_{LB} and V_{RB} . Here, the source–drain bias energy is set to $eV_{SD} = 300$ μeV such

that it exceeds the expected zero-field superconducting gap energy of ~70 μeV (ref. 21). We set V_{LB} close to its pinch-off value such that it acts as a tunnel probe, and we vary V_{RB} to tune the coupling between SC and QD Γ_s values (Fig. 1c). This limits current through the device to around 1 nA, which we estimate to be well within the critical current density of the SCs (Supplementary Fig. 6b). Figure 1e–g shows bias spectroscopy at different values of V_{RB} . In the strong coupling regime (Fig. 1e), we observe a range in bias energy of $4\Delta_0$ where transport is suppressed, from which we extract a superconducting pairing amplitude of $\Delta_0 = 71 \pm 6$ μeV, in its fully open state. The apparent reduction of the SC gap upon lowering the plunger gate voltage V_{PG} is attributed to sub-gap transport phenomena due to increased junction transparency⁴⁵. We furthermore note that the dark features outside of the SC gap likely result from the out-of-gap structure in the SCs⁴⁶. Figure 1f shows that as Γ_s is decreased (positive change in V_{RB}), we observe tunnel-broadened Coulomb oscillations and sub-gap transport features, indicating a hybridized QD. At low coupling between the QD and SC (Fig. 1g) we observe sharp Coulomb diamonds outside a bias window of $\pm 2\Delta_0$. We conclude that we have versatile electrostatic control of the degree of hybridization of a QD with a superconductor, consistent with experiments performed in InAs–Al nanowires⁴⁷ and InSbAs–Al 2D electron gases (ref. 5).

A QD coupled to a SC at half-occupancy of charges can have two different ground states, depending on the degree of SC–QD coupling. At low coupling strengths and zero magnetic field strength, the ground state at half-filling, that is, $\epsilon_0/U = 0.5$, will be a spin-degenerate doublet state $|D\rangle = \{|\downarrow\rangle, |\uparrow\rangle\}$. Here, ϵ_0 is the electrochemical potential of the QD with respect to the SC and U is the charging energy of the QD. At high coupling, a preference for superconducting pairing will dominate, leading to a singlet ground state $|S\rangle = u|0\rangle - v|2\rangle$, where u and v are complex constants. We stress that the labelling of these states is not representative of the localization of the charges between superconductor and QD, and rather a convenient pedagogical representation of the basis states of the system. As a result of U being the dominant energy scale, the system is firmly in the YSR limit. By using the control of Γ_s demonstrated above, we show that we can tune between these ground states. We operate in a regime whereby V_{LB} is very close to its pinch-off value, such that it acts as a tunnelling probe. We then vary V_{RB} to tune the coupling Γ_s . Figure 2a shows a charge stability diagram of the system with the QD plunger gate V_{PG} on the horizontal axis, and the QD–SC barrier gate V_{RB} on the vertical axis, at a bias energy of $eV_{SD} = 80$ μeV, slightly above the SC order parameter, Δ . The vertical lines measured are Coulomb resonances indicating transitions between the N , $N+1$ and $N+2$ occupations of the QD (from right to left). As we increase Γ_s by making V_{RB} more negative, we observe the merging of two levels at approximately $V_{RB} = -1.395$ V.

We further investigate these transitions with bias spectroscopy as a function of plunger gate voltage at different values of V_{RB} . In the bottom panel of Fig. 2b, we show bias spectroscopy at $V_{RB} = -1.3717$ V (square in Fig. 2a) for varying V_{SD} and V_{PG} values. At V_{PG} values of -1.812 V and -1.808 V, the state crosses Δ_0 , signalling the changes in ground state parity as seen from Fig. 2a.

In the bottom panel of Fig. 2c, we show spectroscopy at $V_{RB} = -1.3850$ V (circle in Fig. 2a). We see an evolution of the state features into a characteristic ‘eye’ shape, indicating the formation of YSR states^{38,48} on the hybridized QD. The negative differential conductance is attributed to probing sub-gap features with a coherence peak⁴⁹. In the bottom panel of Fig. 2d, we perform bias spectroscopy at $V_{RB} = -1.4025$ V (triangle in Fig. 2a), showing no parity change, which we interpret as the QD remaining in a singlet ground state upon loading an additional hole.

In QD–SC systems, where the charging energy of the QD, U , is larger than the SC order parameter Δ , quasiparticles in the SC can bind to the QD by the exchange interaction and give rise to sub-gap excitations in the form of YSR states. Such systems can be modelled using a ZBW

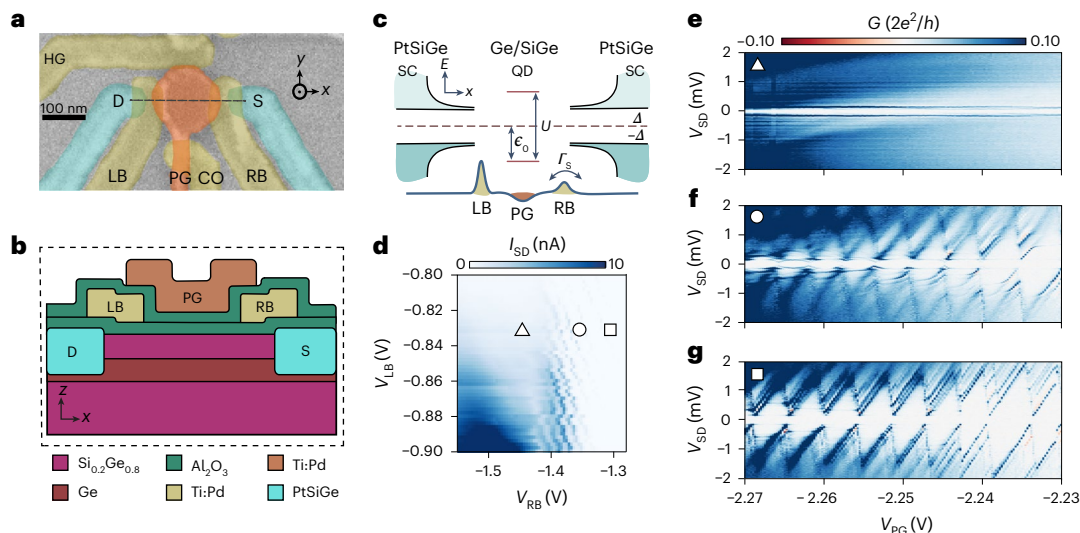


Fig. 1 | Hybrid superconducting PtSiGe-Ge/SiGe device. **a**, False-coloured scanning electron micrograph of a nominally identical device. The device comprises three lithographically defined metallic layers, separated by a dielectric of Al_2O_3 , grown using atomic layer deposition. A plunger gate PG (orange) controls the electrochemical potential of the QD. The coupling of the QD to the PtSiGe SCs (S and D) is controlled by two barrier gates, LB and RB (yellow). A cut-off gate CO prevents accumulation beneath the gate fan-out of PG, and a helper gate HG provides further control of the QD confinement. **b**, Heterostructure and gate stack schematic corresponding to the cross-section indicated by the black dashed line in **a**. **c**, Energy schematic depicting the physical system in **a**. Here, Δ is the SC gap energy, U is the charging energy of the QD,

Γ_s is the hybridization energy of the SC and QD and ϵ_0 is the electrochemical potential of the QD with respect to the SC Fermi energy. The inset axis depicts energy (E) versus space (x) along the line-cut in **a**. **d**, Source-drain current I_{SD} as a function of barrier gates V_{LB} and V_{RB} at bias voltage $V_{SD} = 300 \mu\text{V}$, $V_{PG} = -2.22 \text{ V}$ and $V_{HG} = -1.00 \text{ V}$. The square, circle and triangle correspond to the indicated gate voltage setting in **e**, **f** and **g**. Horizontal features likely correspond to charge instabilities in the environment surrounding the QD. **e-g**, Bias spectroscopy for the three gate voltages indicated in **d**, with high, moderate and low coupling of the QD to the SCs, respectively, showing a transition between strongly coupled lead (**e**) and weakly coupled lead (**g**). Negative differential conductance observed may indicate Coulomb diamonds of odd occupancy⁶⁴.

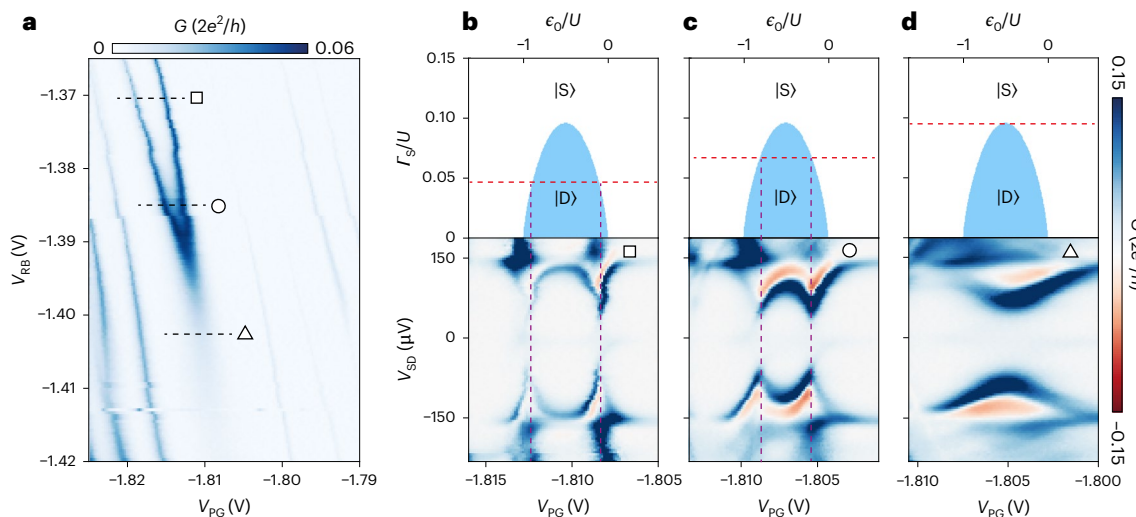


Fig. 2 | Singlet-doublet phase transitions. **a**, Charge stability diagram of V_{RB} versus V_{PG} at $V_{SD} = 80 \mu\text{V}$, $V_{LB} = -1.108 \text{ V}$ and $V_{HG} = -1.000 \text{ V}$. A cross-capacitance between the electrostatic gate V_{RB} and the QD results in simultaneous tuning of Γ_s and ϵ_0 . We note that we expect the QD system to be in the multi-hole regime. **b-d**, Bottom panels show bias spectroscopy at decreasing values of V_{RB} corresponding to the square, circle and triangle icons in **a**. Upper panels portray phase diagrams for the singlet and doublet phases, computed using a minimal ZBW model of the expected ground state character of the hybrid system. Here,

ϵ_0 is the electrochemical potential of the QD with respect to the grounded SCs, and U is the charging energy of the QD; the phase diagram was computed assuming $U = 1.6 \text{ meV}$ and $\Delta = 71 \mu\text{eV}$. As the SC-QD coupling Γ_s is increased, the doublet state becomes energetically unfavourable, as seen by the merging of charge transitions (magenta dashed lines). Γ_s is roughly estimated, by modelling the sub-gap spectrum in the bottom panels (Supplementary Section V), to be 70 μeV , 110 μeV and 150 μeV from **b-d**, respectively, as indicated by the red dashed lines.

model that describes a QD coupled to a single superconducting orbital^{41,50}, which predicts which ground state the system prefers depending on the degree of hybridization between the SC and the QD. By solving the ZBW model for the location where the energy of the singlet equals that of the doublet, a singlet-doublet phase transition diagram can be realized. In the top panels of Fig. 2b-d such a phase

transition has been computed using a ZBW model with a charging energy of $U = 1.6 \text{ meV}$ and a superconducting gap of $\Delta = 71 \mu\text{eV}$; the dashed lines have been inserted at Γ_s values based on extracted coupling values (70 μeV , 110 μeV and 150 μeV , respectively) divided by U , also using the aforementioned minimal ZBW model (Supplementary Section V). As the hybridization energy Γ_s increases, it becomes less

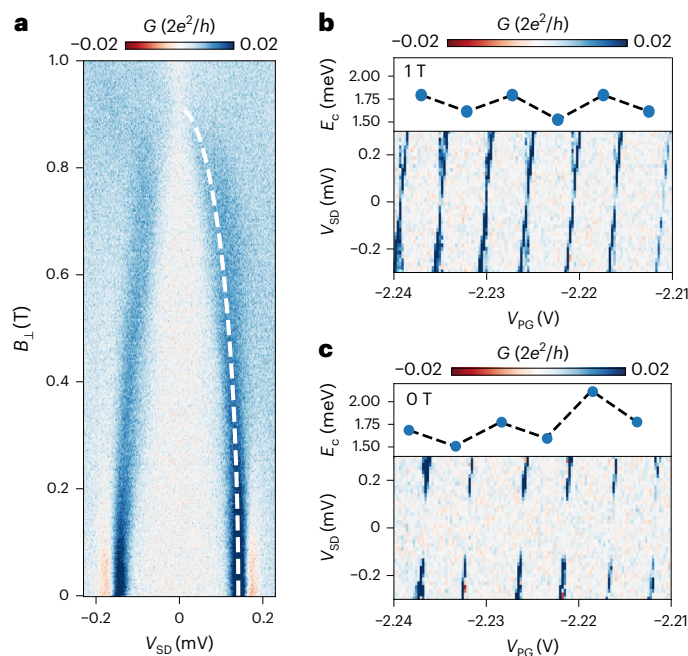


Fig. 3 | Critical field characterization. **a**, Bias spectroscopy as a function of out-of-plane magnetic field B_{\perp} , with $V_{PG} = -2.225$ V, $V_{HG} = 1.000$ V, $V_{RB} = -1.450$ V and $V_{LB} = -0.825$ V. We extract a critical field $B_{c,\perp} = 0.90 \pm 0.04$ T. **b,c**, Bias spectroscopy at low Γ_s values, with $V_{RR} = -1.300$ V, $V_{LB} = -0.825$ V and $V_{HG} = -1.000$ V for out-of-plane magnetic field $B_{\perp} = 1$ T (**b**) and $B_{\perp} = 0$ T (**c**). Top panels show extracted charging energies (E_c) from Coulomb diamonds below.

favourable to maintain the $|D\rangle$ ground state. The horizontal dashed lines thus indicate a qualitative correspondence between the experimental barrier gate RB controlling Γ_s , and the calculated Γ_s in the phase diagram. The magenta dashed lines in the bottom panels serve as guides to the eye to indicate where the phase transitions occur.

We now turn to the magnetic field dependence of the superconducting parent gap. Figure 3a shows bias spectroscopy of the QD in the few-hole and low- Γ_s regime, as a function of out-of-plane magnetic field strength B_{\perp} . We fit the closing of the superconducting gap according to $\Delta(B) = 2\Delta_0\sqrt{1 - (B/B_c)^2}$ (ref. 51), where B is the magnetic field, Δ_0 is the superconducting gap at zero magnetic field and B_c is the critical magnetic field. We extract a critical field of $B_{c,\perp} = 0.90 \pm 0.04$ T. This greatly exceeds the critical field measured in prior studies, where the critical out-of-plane magnetic field was measured to be approximately 50 mT (ref. 21). This disparity could be due to the smaller size of the superconducting junctions and leads⁵² measured in the present experiment compared to those in the literature²¹, which may alleviate vortex formation (Supplementary Section IV.). We also characterize the critical magnetic field strengths for the two in-plane axes in Supplementary Section III. Figure 3b,c shows bias spectroscopy of the QD in the low-coupling limit, taken at 1 T and 0 T, respectively. At 0 T the superconducting gap is present within the Coulomb diamonds (Fig. 3b), while normal Coulomb diamonds are recovered at 1 T due to the breaking down of superconductivity (Fig. 3c). In both cases we find an even-odd oscillation in the filling structure at both low and high field strengths as seen in the top panels of Fig. 3b,c, depicting the addition energy of each Coulomb diamond below, consistent with that observed previously in germanium⁵³ and InAs (ref. 48) QDs. The charging energy of the QD varies between even and odd periodicity, indicating that the QD is in the low hole occupancy state. The charging energy is typically between 1 and 1.8 meV, more than ten times the superconducting gap, supporting our interpretation that we are in the YSR regime.

Finally we study the transport spectrum under the influence of a magnetic field in the same electrostatic regime as Fig. 2b,c. Figure 4a–c

shows bias spectroscopy measurements as a function of V_{PG} portrayed in logarithmic scale for enhanced visibility, taken at a perpendicular magnetic field, at strengths of 50 mT, 250 mT and 350 mT, respectively (Supplementary Fig. 7a–c for data in non-logarithmic scale). At 50 mT, a $|S\rangle - |D\rangle - |S\rangle$ transition spectrum is observed, as seen in Fig. 2b,c. A qualitative ZBW model of the system is plotted on top of the data (dashed white line), as described previously (Supplementary Section V for details of the model), using a SC pairing energy of $\Delta_0 = 71$ μ eV, a hybridization energy of $\Gamma_s = 110$ μ eV and a QD charging energy of $U = 1.6$ meV. As we increase the perpendicular field, an energy splitting of the sub-gap states is observed in the singlet ground-state sectors (Fig. 4b,c). Interestingly, the energy splittings seen in the even-parity ground states have a flat energy dispersion, indicating a spin splitting either of the parent gap itself, or of a strongly coupled sub-gap state, which we attribute to spinful excited quasiparticles. To qualitatively model the data, we introduce a Zeeman splitting term into the ZBW model for both the SC and QD. We find that setting the g-factors of the QD and superconducting orbitals to be equal in magnitude is sufficient to phenomenologically model the data, potentially due to a g-factor renormalization as a result of hybridization^{54,55}. Additional data at lower magnetic field strength and lower coupling, supporting our hypothesis of g-factor renormalization, are reported in Supplementary Section II, as well as results from our ZBW model with varying system parameters in Supplementary Section V.

In Fig. 4d, we set the plunger gate voltage to $V_{PG} = -1.8027$ V such that the QD is in a singlet ground state as indicated by the red notch in Fig. 4a, and perform bias spectroscopy as a function of B_{\perp} from 0 T to 0.7 T. We observe the magnetic field splitting of the superconducting coherence peaks, and extract an out-of-plane g-factor, $g_{\perp} = 1.5 \pm 0.2$. This value is several times larger than the g-factor measured for magnetic fields close to being in plane, in planar germanium quantum wells^{56,57}, and several times smaller than the value reported in the literature⁵⁸ for out-of-plane g-factors. Furthermore, in a regime of lower coupling for the YSR states, we measured an out-of-plane g-factor of $g_{\perp} = 4.5 \pm 0.6$ (Supplementary Fig. 2) and a $g_{\perp} = 5.3 \pm 0.8$ in out-of-gap Coulomb diamond spectroscopy (Supplementary Fig. 3). These observations support the hypothesis that the g-factor g_{\perp} either describes the quasiparticle coherence peaks, or is due to renormalization of the Ge/SiGe hole g-factor as a result of hybridization with the superconductor^{54,55}.

Finally, we investigate anisotropy of the g-factor by performing bias spectroscopy as a function of magnetic field orientation. Figure 4e–g shows bias spectroscopy at a magnetic field strength of $|B| = 420$ mT. The splitting is then investigated as a function of rotation angles. Here, the rotation angles θ, ϕ and α are defined as shown in Fig. 4e–g. A large anisotropy is measured; while g-tensor anisotropy is ubiquitous for heavy holes in strained planar Ge/SiGe wells, it is seldom observed for a superconducting gap edge. On the other hand, anisotropic g-tensors have been observed in heavy fermion bulk superconductors, which could additionally explain the non-dispersive splitting in Fig. 4b,c (ref. 59). We stress that our use of the annealed polycrystalline superconductor PtSiGe is a recent material development in itself, and the physics of superconductivity in these nanoscale thin films is not fully understood. However, this anisotropy could also be explained by a sub-gap state in the QD that is strongly coupled to the superconductor.

We have demonstrated a QD in Ge/SiGe proximitized by a SC and exhibiting clear YSR states. We find that the coupling between QD and SC is highly tunable, as evidenced by the tunnel barrier controllability of the singlet or doublet nature of the YSR ground state at half filling. Additionally, we have characterized the critical magnetic field strength, finding an out-of-plane critical field of -0.90 T. Finally, we observe Zeeman splitting of sub-gap states, which we explain using a modified ZBW Anderson impurity model. The ability to tune and strongly couple a superconductor to a QD, in combination with a critical magnetic field, demonstrates the feasibility of our platform for hybrid

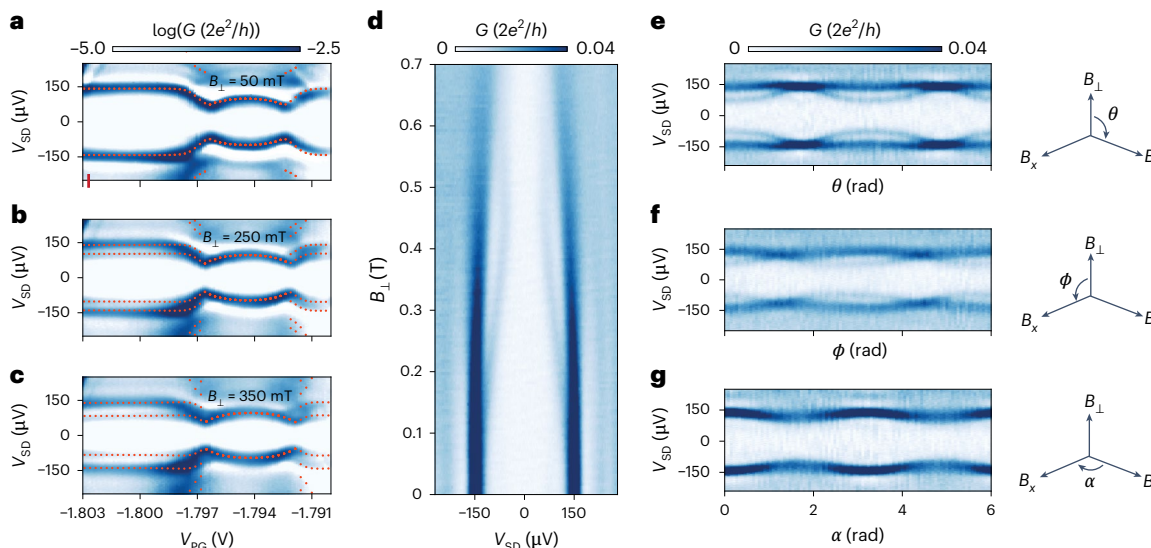


Fig. 4 | Hybridized g-factor spectroscopy. **a–c**, Bias spectroscopy displayed in logarithmic scale at magnetic field strengths of 50 mT, 250 mT and 350 mT, respectively, with the barrier gates set to $V_{RB} = -1.4100$ V, $V_{LB} = -0.8070$ V and $V_{HG} = -0.9575$ V. Sub-gap energy splitting is visible in **b** and **c**. The superimposed orange markers in **a–c** serve as a qualitative comparison between the measured transport data and calculations using a ZBW model, inputting $\Delta = 71$ μeV, hybridization energy $\Gamma_s = 110$ μeV and charging energy $U = 1.6$ meV, as well as a Zeeman energy (E_Z) of $E_Z^{\text{SC}} = 4$ μeV on the SC and $E_Z^{\text{QD}} = 4$ μeV on the QD; $E_Z^{\text{SC}} = 44$ μeV on the SC and $E_Z^{\text{QD}} = 44$ μeV on the QD; and $E_Z^{\text{SC}} = 56$ μeV on the SC

and $E_Z^{\text{QD}} = 56$ μeV on the QD, respectively for **a** through **c**. **d**, Magnetic field sweep at $V_{RB} = -1.4100$ V, $V_{LB} = -0.8070$ V, $V_{HG} = -0.9575$ V and $V_{PG} = -1.8027$ V tuned within the singlet ground state, as indicated by the red notch in **a**. We extract a g-factor for the out-of-plane magnetic field splitting $g_{\perp} = 1.5 \pm 0.2$. **e–g**, Bias spectroscopy of rotating magnetic field at total magnetic field strength $|B| = 420$ mT and $V_{PG} = -1.8028$ V, also tuned to the singlet ground state. Strong g-tensor anisotropy is observed between out-of-plane and in-plane magnetic field orientations (B_x and B_y), as defined by the coordinate system in Fig. 1a.

germanium quantum information processing, including Andreev spin qubits and topological quantum computing, as well as the exploration of fundamental physics with superconductor–semiconductor devices. While the in-plane g-tensor component of holes in germanium planar wells is lower than in established group III–V platforms, it could be enhanced by confinement-induced g-factor engineering⁶⁰, and the out-of-plane g-factor could provide an alternative route to engineering topologically protected qubits using QD–SC chains⁶¹. Further work on radiofrequency-reflectometry-based measurements (as described in Supplementary Sections I and II) could help achieve charge sensing and parity readout. Additionally, studying the dependence of the parent gap and induced gap as a function of temperature and coupling strength would elucidate the nature of the superconducting proximitization of PtSiGe on Ge/SiGe QDs⁴⁵. Finally, our work motivates the exploration of alternative materials beyond platinum that also form superconducting germanide phases, such as iridium, rhodium⁶² and niobium⁶³, with the goal of identifying a germanosilicide capable of hosting large superconducting gap energies while being compatible with the fabrication process of Ge/SiGe heterostructures⁴³. Our demonstration in a group IV material, amenable to isotopic purification, constitutes a crucial building block for superconducting–semiconducting hybrid technologies and opens up previously inaccessible experimental directions.

Online content

Any methods, additional references, Nature Portfolio reporting summaries, source data, extended data, supplementary information, acknowledgements, peer review information; details of author contributions and competing interests; and statements of data and code availability are available at <https://doi.org/10.1038/s41563-024-02095-5>.

References

1. Böttcher, C. G. L. et al. Superconducting, insulating and anomalous metallic regimes in a gated two-dimensional semiconductor–superconductor array. *Nat. Phys.* **14**, 1138–1144 (2018).
2. Hays, M. et al. Coherent manipulation of an Andreev spin qubit. *Science* **373**, 430–433 (2021).
3. Bargerbos, A. et al. Spectroscopy of spin-split Andreev levels in a quantum dot with superconducting leads. *Phys. Rev. Lett.* **131**, 097001 (2023).
4. Leijnse, M. & Flensberg, K. Parity qubits and poor man’s Majorana bound states in double quantum dots. *Phys. Rev. B* **86**, 134528 (2012).
5. ten Haaf, S. L. D. et al. Engineering Majorana bound states in coupled quantum dots in a two-dimensional electron gas. Preprint at <https://doi.org/10.48550/arXiv.2311.03208> (2023).
6. Dvir, T. et al. Realization of a minimal Kitaev chain in coupled quantum dots. *Nature* **614**, 445–450 (2023).
7. Wang, G. et al. Singlet and triplet Cooper pair splitting in hybrid superconducting nanowires. *Nature* **612**, 448–453 (2022).
8. Pino, D. M., Souto, R. S. & Aguado, R. Minimal Kitaev-transmon qubit based on double quantum dots. *Phys. Rev. B* **109**, 075101 (2024).
9. Wang, Q. et al. Triplet correlations in Cooper pair splitters realized in a two-dimensional electron gas. *Nat. Commun.* **14**, 4876 (2023).
10. Scigliuzzo, M. et al. Phononic loss in superconducting resonators on piezoelectric substrates. *New J. Phys.* **22**, 053027 (2020).
11. Burkard, G., Ladd, T. D., Pan, A., Nichol, J. M. & Petta, J. R. Semiconductor spin qubits. *Rev. Mod. Phys.* **95**, 025003 (2023).
12. Scappucci, G. et al. The germanium quantum information route. *Nat. Rev. Mater.* **6**, 926–943 (2021).
13. Muhonen, J. T. et al. Storing quantum information for 30 seconds in a nanoelectronic device. *Nat. Nanotechnol.* **9**, 986–991 (2014).
14. Tao, M. et al. Low Schottky barriers on n-type silicon (001). *Appl. Phys. Lett.* **83**, 2593–2595 (2003).
15. Dimoulas, A., Tsipas, P., Sotiropoulos, A. & Evangelou, E. K. Fermi-level pinning and charge neutrality level in germanium. *Appl. Phys. Lett.* **89**, 252110 (2006).

16. Nishimura, T., Kita, K. & Toriumi, A. Evidence for strong Fermi-level pinning due to metal-induced gap states at metal/germanium interface. *Appl. Phys. Lett.* **91**, 123123 (2007).

17. Aggarwal, K. et al. Enhancement of proximity-induced superconductivity in a planar Ge hole gas. *Phys. Rev. Res.* **3**, L022005 (2021).

18. Vigneau, F. et al. Germanium quantum-well Josephson field-effect transistors and interferometers. *Nano Lett.* **19**, 1023–1027 (2019).

19. Hendrickx, N. W. et al. Gate-controlled quantum dots and superconductivity in planar germanium. *Nat. Commun.* **9**, 2835 (2018).

20. Ridderbos, J. et al. Josephson effect in a few-hole quantum dot. *Adv. Mater.* **30**, 1802257 (2018).

21. Tosato, A. et al. Hard superconducting gap in germanium. *Commun. Mater.* **4**, 23 (2023).

22. Valentini, M. et al. Parity-conserving Cooper-pair transport and ideal superconducting diode in planar germanium. *Nat. Commun.* **15**, 169 (2024).

23. Ridderbos, J. et al. Hard superconducting gap and diffusion-induced superconductors in Ge–Si nanowires. *Nano Lett.* **20**, 122–130 (2020).

24. Zhuo, E. et al. Hole-type superconducting gatemon qubit based on Ge/Si core/shell nanowires. *npj Quantum Inf.* **9**, 51 (2023).

25. Zheng, H. et al. Coherent control of a few-channel hole type gatemon qubit. *Nano Lett.* **24**, 7173–7179 (2024).

26. Hinderling, M. et al. Direct microwave spectroscopy of Andreev bound states in planar Ge Josephson junctions. *PRX Quantum* **5**, 030357 (2024).

27. Itoh, K. et al. High purity isotopically enriched ^{70}Ge and ^{74}Ge single crystals: isotope separation, growth, and properties. *J. Mater. Res.* **8**, 1341–1347 (1993).

28. Vigneau, F. et al. Probing quantum devices with radio-frequency reflectometry. *Appl. Phys. Rev.* **10**, 021305 (2023).

29. Hendrickx, N. W. et al. A four-qubit germanium quantum processor. *Nature* **591**, 580–585 (2021).

30. Jirovec, D. et al. A singlet-triplet hole spin qubit in planar Ge. *Nat. Mater.* **20**, 1106–1112 (2021).

31. Leijnse, M. & Flensberg, K. Coupling spin qubits via superconductors. *Phys. Rev. Lett.* **111**, 060501 (2013).

32. Spethmann, M., Bosco, S., Hofmann, A., Klinovaja, J. & Loss, D. High-fidelity two-qubit gates of hybrid superconducting-semiconducting singlet-triplet qubits. *Phys. Rev. B* **109**, 085303 (2024).

33. Gynis, A. et al. Moving beyond the transmon: noise-protected superconducting quantum circuits. *PRX Quantum* **2**, 030101 (2021).

34. Kjaergaard, M. et al. Superconducting qubits: current state of play. *Annu. Rev. Condens. Matter Phys.* **11**, 369–395 (2020).

35. Bai, M. et al. Novel self-epitaxy for inducing superconductivity in the topological insulator $(\text{Bi}_{1-x}\text{Sb}_x)_2\text{Te}_3$. *Phys. Rev. Mater.* **4**, 094801 (2020).

36. Rosen, I. T. et al. Fractional AC Josephson effect in a topological insulator proximitized by a self-formed superconductor. *Phys. Rev. B* **110**, 064511 (2024).

37. Jia, Y. et al. Superconductivity from on-chip metallization on 2D topological chalcogenides. *Phys. Rev. X* **14**, 021051 (2024).

38. Kirsanskas, G., Goldstein, M., Flensberg, K., Glazman, L. I. & Paaske, J. Yu-Shiba-Rusinov states in phase-biased superconductor–quantum dot–superconductor junctions. *Phys. Rev. B* **92**, 235422 (2015).

39. Jellinggaard, A., Grove-Rasmussen, K., Madsen, M. H. & Nygaard, J. Tuning Yu-Shiba-Rusinov states in a quantum dot. *Phys. Rev. B* **94**, 064520 (2016).

40. Bargerbos, A. et al. Singlet-doublet transitions of a quantum dot Josephson junction detected in a transmon circuit. *PRX Quantum* **3**, 030311 (2022).

41. Bauer, J., Oguri, A. & Hewson, A. C. Spectral properties of locally correlated electrons in a Bardeen-Cooper-Schrieffer superconductor. *J. Phys. Condens. Matter* **19**, 486211 (2007).

42. Meng, T., Florens, S. & Simon, P. Self-consistent description of Andreev bound states in Josephson quantum dot devices. *Phys. Rev. B* **79**, 224521 (2009).

43. Lawrie, W. I. L. et al. Quantum dot arrays in silicon and germanium. *Appl. Phys. Lett.* **116**, 080501 (2020).

44. Sammak, A. et al. Shallow and undoped germanium quantum wells: a playground for spin and hybrid quantum technology. *Adv. Funct. Mater.* **29**, 1807613 (2019).

45. Kjaergaard, M. et al. Transparent semiconductor-superconductor interface and induced gap in an epitaxial heterostructure Josephson junction. *Phys. Rev. Appl.* **7**, 034029 (2017).

46. Su, Z. et al. Mirage Andreev spectra generated by mesoscopic leads in nanowire quantum dots. *Phys. Rev. Lett.* **121**, 127705 (2018).

47. Lee, E. J. H. et al. Spin-resolved Andreev levels and parity crossings in hybrid superconductor–semiconductor nanostructures. *Nat. Nanotechnol.* **9**, 79–84 (2014).

48. Grove-Rasmussen, K. et al. Superconductivity-enhanced bias spectroscopy in carbon nanotube quantum dots. *Phys. Rev. B* **79**, 134518 (2009).

49. Andersen, B. M., Flensberg, K., Koerting, V. & Paaske, J. Nonequilibrium transport through a spinful quantum dot with superconducting leads. *Phys. Rev. Lett.* **107**, 256802 (2011).

50. Baran, V. V., Frost, E. J. & Paaske, J. Surrogate model solver for impurity-induced superconducting subgap states. *Phys. Rev. B* **108**, L220506 (2023).

51. Tinkham, M. *Introduction to Superconductivity* 2nd edn (Dover Publications, 2004).

52. Fulde, P. High field superconductivity in thin films. *Adv. Phys.* **22**, 667–719 (1973).

53. van Riggelen, F. et al. A two-dimensional array of single-hole quantum dots. *Appl. Phys. Lett.* **118**, 044002 (2021).

54. de Moor, M. W. A. et al. Electric field tunable superconductor–semiconductor coupling in Majorana nanowires. *New J. Phys.* **20**, 103049 (2018).

55. Antipov, A. E. et al. Effects of gate-induced electric fields on semiconductor Majorana nanowires. *Phys. Rev. X* **8**, 031041 (2018).

56. Hendrickx, N. W., Franke, D. P., Sammak, A., Scappucci, G. & Veldhorst, M. Fast two-qubit logic with holes in germanium. *Nature* **577**, 487–491 (2020).

57. Hendrickx, N. W. et al. A single-hole spin qubit. *Nat. Commun.* **11**, 3478 (2020).

58. Hendrickx, N. W. et al. Sweet-spot operation of a germanium hole spin qubit with highly anisotropic noise sensitivity. *Nat. Mater.* **23**, 920–927 (2024).

59. Chandra, P., Coleman, P. & Flint, R. Haptic order in the heavy-fermion compound URu_2Si_2 . *Nature* **493**, 621–626 (2013).

60. Bosco, S., Benito, M., Adelsberger, C. & Loss, D. Squeezed hole spin qubits in Ge quantum dots with ultrafast gates at low power. *Phys. Rev. B* **104**, 115425 (2021).

61. Laubscher, K., Sau, J. D. & Das Sarma, S. Germanium-based hybrid semiconductor-superconductor topological quantum computing platforms: disorder effects. *Phys. Rev. B* **110**, 155431 (2024).

62. Matthias, B. T., Geballe, T. H. & Compton, V. B. Superconductivity. *Rev. Mod. Phys.* **35**, 1–22 (1963).

63. Langa, B. et al. Solid-state reactions at niobium-germanium interfaces in hybrid superconductor–semiconductor devices. *AIP Adv.* **14**, 095311 (2024).

64. De Franceschi, S., Kouwenhoven, L., Schoenenberger, C. & Wernsdorfer, W. Hybrid superconductor–quantum dot devices. *Nat. Nanotechnol.* **5**, 703–711 (2010).

Publisher's note Springer Nature remains neutral with regard to jurisdictional claims in published maps and institutional affiliations.

Open Access This article is licensed under a Creative Commons Attribution-NonCommercial-NoDerivatives 4.0 International License, which permits any non-commercial use, sharing, distribution and reproduction in any medium or format, as long as you give appropriate credit to the original author(s) and the source, provide a link to the Creative Commons licence, and indicate if you modified the licensed material. You do not have permission under this licence to share

adapted material derived from this article or parts of it. The images or other third party material in this article are included in the article's Creative Commons licence, unless indicated otherwise in a credit line to the material. If material is not included in the article's Creative Commons licence and your intended use is not permitted by statutory regulation or exceeds the permitted use, you will need to obtain permission directly from the copyright holder. To view a copy of this licence, visit <http://creativecommons.org/licenses/by-nc-nd/4.0/>.

© The Author(s) 2025

Methods

The device is fabricated on a Ge/SiGe heterostructure, which is grown on an n-type Si(001) substrate using a reduced pressure chemical vapour deposition reactor. The stack comprises a reverse-graded $\text{Si}_{0.2}\text{Ge}_{0.8}$ virtual substrate, a 16 nm Ge quantum well, a 27 nm $\text{Si}_{0.2}\text{Ge}_{0.8}$ barrier and a <1 nm Si sacrificial cap⁴⁴. The device is fabricated in three defined electron-beam lithography layers separated by two oxide layers of ~ 7 nm Al_2O_3 grown with a Savannah Ultratech atomic layer deposition system at 150 °C, using unheated trimethyl aluminium precursor and unheated H_2O thermal co-reactant. The first layer forms the PtSiGe contacts defined by electron-beam lithography using Kayaku 495 polymethyl methacrylate A2 polymer resist and AR 600-55 1:3 MIBK/IPA developer (MIBK, methyl isobutyl ketone; IPA, isopropyl alcohol). Development is directly followed by a 60 s, 100 °C post bake on a hot plate before a wet etch is performed using buffered HF ($\sim 6\%$) solution to remove the sacrificial cap before a 15 nm Pt layer is deposited via electron-gun evaporation at a pressure of 1×10^{-7} mbar. Lift-off is done in *N*-methyl-2-pyrrolidone, followed by 1,2-dioxolane and then propan-2-ol (IPA) cleaning. The Pt contacts then undergo rapid thermal annealing at 400 °C for 15 min in an argon atmosphere. Barrier gates and plunger gates are defined by electron-beam lithography using AR-P 6200.04 polymer resist and *N*-amyl acetate developer, followed by an oxygen plasma ash. The barrier and plunger gates are deposited using electron-gun evaporation and consist of a Ti (5 nm) sticking layer and a Pd layer (25 nm and 29 nm for the barrier and plunger layers, respectively). Lift-off is done in 1,2-dioxolane, followed by 1,2-dioxolane, propan-2-ol (IPA) and oxygen plasma ash cleaning.

The device is measured inside a sample puck loaded into a Bluefors XLD dilution refrigerator, at a mixing chamber temperature of ~ 9 mK. The dilution refrigerator is equipped with a 1 T–1 T–6 T vector magnet, the sample chip being placed such that the 6 T direction is in the plane. We expect the main source of magnetic field misalignment to result from misalignment of the sample board inside the puck (QDevil QBoard sample holder) during sample loading. We estimate this error to be less than 5° .

Differential conductance measurements are taken using a Stanford Research Systems SR860 lock-in amplifier at a frequency of 119 Hz and an excitation amplitude (V_{AC}) of 2.5 μV for all figures, except Fig. 2a ($V_{\text{AC}} = 10$ μV) and Fig. 4 ($V_{\text{AC}} = 3.2$ μV). A line resistance of ~ 5.8 $\text{k}\Omega$ is subtracted in all measurements.

Bias spectroscopy measurements contain small thermally induced bias offsets on the order of 20 μeV , which have been calibrated for and subtracted from all relevant datasets. The d.c. gate voltages are applied via a QDevil QDAC-II voltage source. Additional information on the d.c. set-up and components used can be found in Supplementary Section I.

In addition to lock-in measurements, radiofrequency reflectometry was performed as described in Supplementary Section I, using a field-programmable gate array with a built-in microwave signal generator as well as signal demodulator (Quantum Machines OPX+). A tank circuit with a resonance frequency of 192.3 MHz was used, connected to the drain contact. The incident radiofrequency signal is attenuated by 40 dB at various plates of the cryostat, and undergoes an additional attenuation of 20 dB from a directional coupler at the mixing chamber plate (Supplementary Fig. 1). The reflected signal undergoes 40 dB of amplification at the 4 K stage via a high electron mobility transistor

(HEMT) amplifier, and passes through a d.c. block and bias tee at the input of the demodulation circuit. A $50\ \Omega$ terminator is connected to the d.c. side of the bias tee.

Data availability

Raw data are available via Zenodo at <https://doi.org/10.5281/zenodo.11088753> (ref. 65).

Code availability

Analysis scripts for all data included in this work are available via Zenodo at <https://doi.org/10.5281/zenodo.11088753> (ref. 65). These scripts aid in plotting and viewing the data, as well as generating the simulations in the main text and supplementary information.

References

65. Lakic, L. et al. Dataset underlying the manuscript: a proximitized quantum dot in germanium. Zenodo <https://doi.org/10.5281/zenodo.11088753> (2024).

Acknowledgements

We thank J. Paaske, V. Baran and G. Mazur for valuable discussions. This project received funding from the European Research Council as part of the project NONLOCAL under grant agreement no. 856526 (F.K.) and through the IGNITE project under grant agreement no. 101069515 of the Horizon Europe Framework Programme (F.K., A.C., M.V. and G.S.). A.C. acknowledges support from the Inge Lehmann Programme of the Independent Research Fund Denmark. D.v.D. acknowledges funding from the Casimir PhD Travel Grant.

Author contributions

L.E.A.S. and G.S. grew and supplied the Ge/SiGe heterostructures and developed processes for the PtSiGe contacts. L.L. and W.I.L.L. designed the devices. L.L. fabricated the devices. L.L. and W.I.L.L. performed the experiment in the dilution refrigerator along with D.v.D. and Y.S., and analysed the data. L.L. performed numerical simulations within the ZBW model with help from D.v.D and W.I.L.L.; L.L. and W.I.L.L. wrote the manuscript with input from D.v.D., M.V., G.S., F.K. and A.C.; and A.C. and F.K. supervised the project.

Competing interests

The authors declare no competing interests.

Additional information

Supplementary information The online version contains supplementary material available at <https://doi.org/10.1038/s41563-024-02095-5>.

Correspondence and requests for materials should be addressed to Anasua Chatterjee.

Peer review information *Nature Materials* thanks the anonymous reviewers for their contribution to the peer review of this work.

Reprints and permissions information is available at www.nature.com/reprints.